Journal of Materials Chemistry A

Accepted Manuscript

ROYAL SOCIETY OF CHEMISTRY

www.rsc.org/materialsA

Journal Name

ARTICLE

Two different mechanisms of $CH_3NH_3PbI_3$ film formation in one-step deposition and its effect on photovoltaic properties of OPV-type perovskite solar cells

Received 00th January 20xx,
Accepted 00th January 20xx

DOI: 10.1039/x0xx00000x

www.rsc.org/

Seunghwan Bae,[a] Seung Jin Han,[a] Tae Joo Shin[b] and Won Ho Jo*[a]

Although one-step deposition method has intensively been studied because of simple and easy fabrication of perovskite films, uncontrolled crystallization of perovskite during one-step deposition often results in films with small crystallites and low surface coverage, leading to low photovoltaic performance. In this study, we have proposed the optimum processing condition to afford favorable crystal morphology of perovskite film for achieving high power conversion efficiency of perovskite solar cells. Two different morphologies, tree-like and flower-like morphologies, are developed depending upon the spin-coating time and post-heat treatment temperature. When the perovskite is crystallized from the liquid film after short spin-coating time, the flower-like morphology is developed, whereas the tree-like morphology is developed when the perovskite is crystallized for long spin-coating time. When the morphology evolution is monitored using in-situ optical microscopy and X-ray diffraction to investigate the origin of the difference between tree-like and flower-like morphologies, it reveals that CH_3NH_3I–PbI_2–solvent complex is formed to develop the tree-like morphology before $CH_3NH_3PbI_3$ crystals are formed whereas the flower-like morphology is developed when the $CH_3NH_3PbI_3$ crystals are formed directly from the liquid film without formation of CH_3NH_3I–PbI_2–solvent complex. The film with flower-like morphology, as prepared from DMSO solution, has large-sized crystallites, and the crystallites are highly orientated along (112) and (200) directions, resulting in a high PCE of 13.85%, whereas the film with tree-like morphology has small-sized crystallites with random crystal orientation, exhibiting very low PCEs.

Introduction

Organic-inorganic perovskites such as $CH_3NH_3PbI_3$, $CH_3NH_3Pb(I_xBr_{1-x})_3$ and $HC(NH_2)_2PbI_3$ are promising light absorbers because they have superior properties including broad light absorption from UV to near-IR range,[1,2] high extinction coefficient,[3,4] long diffusion length of free charge carriers,[5,6] low exciton binding energy[7–9] and excellent charge carrier transport.[10,11] Since perovskite-based photovoltaics have been introduced in 2009 by Kojima *et al.*,[12] a dramatic enhancement of device performance has been achieved.[13]

Although the use of mesoporous scaffold such as TiO_2 or Al_2O_3 for perovskite solar cells has achieved power conversion efficiencies (PCEs) over 11%,[14–17] bilayer structure has recently attracted more interest because of its simple structure and high PCEs comparable to those of meso-structured solar cells.[18–22] Especially, organic photovoltaic (OPV)-type planar devices (TCO/PEDOT:PSS/perovskite/PCBM /Al) have recently been studied because of unique advantage of low-temperature processing compared to dye-sensitized solar cell (DSSC)-type planar devices (TCO/compact-TiO_2 (c-TiO_2)/perovskite/spiro-OMeTAD/Au) in which c-TiO_2 layer requires high temperature sintering (> 450 °C).

In OPV-type planar devices, the morphology control of perovskite film plays a crucial role, and the requirements for the proper morphology of perovskite film to achieve high photovoltaic performance have been proposed: First, good surface coverage of perovskite film reduces the shunting path and also improves the light absorption.[14] Second, perovskite film with large crystal size facilitates the transport of photo-generated charge carriers.[15] Third, low defect density mitigates the hysteresis in the photocurrent (*J*)–voltage (*V*) curve by suppressing the charge trapping.[16–18]

Until now, the mostly used method to fabricate perovskite film is one-step deposition due to cost-effective, simple and easy fabrication, although other fabrication methods such as sequential deposition (two-step deposition)[19] and vacuum deposition[20] have been proposed. However, uncontrolled solidification of perovskite precursor solution during one-step deposition often results in films with low surface coverage[20] and therefore intensive efforts have focused on improving the surface coverage of perovskite film by one-step deposition. Recently, several methods have been reported to control the morphology of perovskite film for the active layer of solar

[a] Department of Materials Science and Engineering, Seoul National University, 1 Gwanak-ro, Gwanak-gu, Seoul, 151-744, Korea
[b] UNIST Central Research Facilities & School of Natural Science, Ulsan National Institute of Science and Technology, 50 UNIST-gil, Eonyang-eup, Ulju-gun,Ulsan, 689-798, Korea

Electronic Supplementary Information (ESI) available: [details of any supplementary information available should be included here]. See DOI: 10.1039/x0xx00000x

cells: the choice of processing solvent,[21–23] the addition of solvent additives,[24–28] anti-solvent washing,[29,30] and fast deposition-crystallization.[15] Consequently, the high power conversion efficiencies (PCEs) over 12% have recently been achieved by one-step deposition.

Herein, we report a simple method to fabricate high quality $CH_3NH_3PbI_3$ film to afford high efficiency perovskite solar cells and also elucidate the difference of film formation mechanism depending upon the processing condition. Finally we propose the optimum processing condition to obtain high quality of perovskite film. The tree-like morphology with many pinholes is developed when the film is fabricated by the conventional one-step deposition, where the solidification due to solvent evaporation is accompanied by crystallization during spin-coating. However, when the spin-coating time is shortened so as to avoid the solidification during spin-coating, $CH_3NH_3PbI_3$ is not crystallized during spin-coating. The liquid film is then crystallized by post heat-treatment at high temperature (110 °C), resulting in flower-like morphology covering the substrate fully without pinholes. Especially, when the perovskite film is fabricated from DMSO solution by spin-coating for short time followed by heat-treatment, the film exhibits flower-like morphology with large crystal size of tens of micrometers and highly preferred crystal orientation to the substrate. The devices with tree-like morphology exhibit low PCEs due to formation of shunting pathway through pinholes, while those with flower-like morphology show remarkably improved PCEs.

Results and discussion

Photovoltaic properties

It has been reported that the perovskite films processed by one-step deposition have low surface coverage with many pinholes due to uncontrolled solidification during spin-coating process.[20] To overcome this problem in this work, the spin-coating time is controlled when the perovskite films are fabricated by one-step deposition of precursor solution (CH_3NH_3I:PbI_2=1:1 molar ratio) using two different solvents, DMF and DMSO. When the current density–voltage (J–V) curves are measured with an OPV-type device configuration of glass/ITO/PEDOT:PSS/$CH_3NH_3PbI_3$/$PC_{61}BM$/Ca/Al under AM1.5G illumination, the open-circuit voltage (V_{OC}), short-circuit current (J_{SC}) and fill factor (FF) are largely improved as the spin-coating time is decreased (Fig. 1 and Table 1). The power conversion efficiency (PCE) of devices fabricated from DMF solution increases from 0.55% to 6.95% as the spin-coating time is decreased from 30 s to 3 s, and the PCE of devices fabricated from DMSO solution also increases from 0.22% to 13.85% as the spin-coating time is decreased from 90 s to 15 s, indicating that the device performance becomes better as the spin-coating time is decreased. It should be noted here that all devices are heat-treated at 110 °C for 30 s after spin-coating. Furthermore, the PCEs of the devices fabricated from the best processing condition exhibit small standard deviation less than 0.4%, indicating that highly efficient perovskite solar

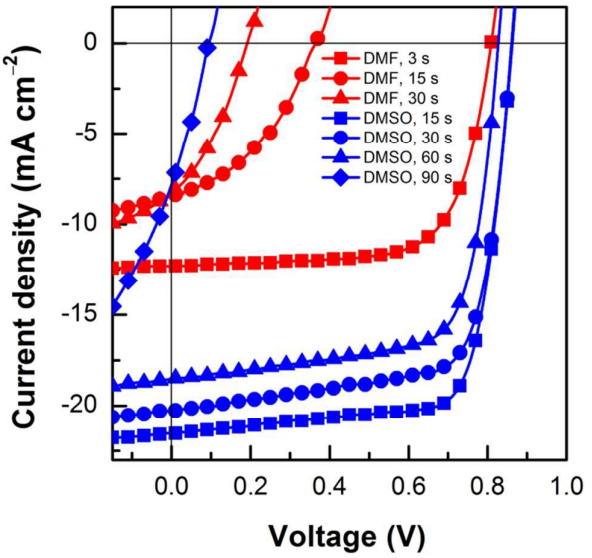

Fig. 1 J–V curves of $CH_3NH_3PbI_3$ perovskite solar cells. The $CH_3NH_3PbI_3$ films in the devices are prepared by spin-coating the DMF and DMSO solutions with different spin-coating times, then are thermally treated at 110 °C for 30 s.

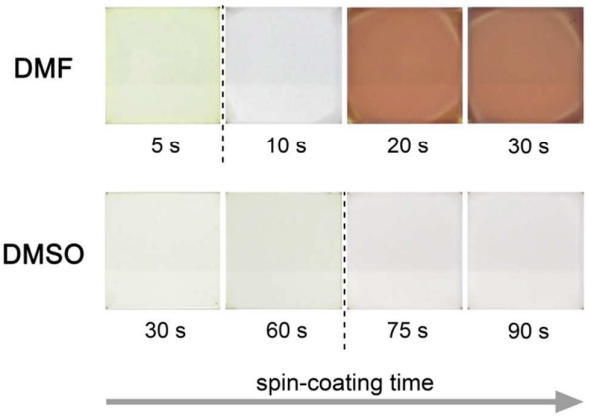

Fig. 2 The change of film state with different spin-coating time using DMF and DMSO solutions before heat treatment. Dashed lines denote the point at which the liquid film starts to solidify.

Table 1 Photovoltaic properties of $CH_3NH_3PbI_3$ perovskite solar cells depending on solvent and spin-coating time

solvent	Spin-coating time [s]	V_{OC} [V]	J_{SC} [mA cm^{-2}]	FF	PCE[a] [%]	Sandard deviation
DMF	3	0.81	12.31	0.70	6.95 (6.68)	0.21
DMF	15	0.36	8.45	0.41	1.23 (0.79)	0.29
DMF	30	0.19	8.28	0.35	0.55 (0.47)	0.09
DMSO	15	0.86	21.55	0.75	13.85 (13.23)	0.37
DMSO	30	0.86	20.31	0.72	12.51 (12.17)	0.38
DMSO	60	0.83	18.50	0.71	10.91 (10.53)	0.29
DMSO	90	0.09	7.82	0.31	0.22 (0.16)	0.03

[a] Average PCE values based on 10 devices are indicated in parentheses.

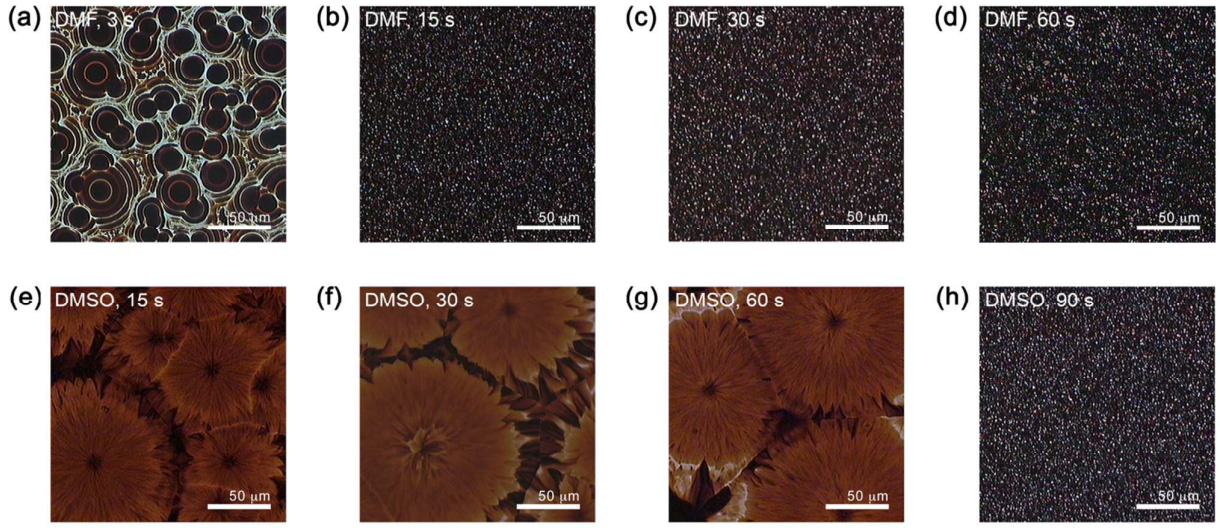

Fig. 3 OM images of $CH_3NH_3PbI_3$ films formed from different solvent and various spin-coating time. The films are fabricated from (a–d) DMF and (e–h) DMSO solution for different spin-coating times. All films are spin-coated at 3000 rpm and are thermally treated at 110 °C for 30 s immediately after spin-coating.

cells can be obtained reproducibly by simply reducing the spin-coating time (Table 1 and Fig. S7). Also, it is interesting to observe that *J*–*V* curves of our devices are hysteresis-less (Fig. S1).

Morphological control

To identify the reason why the devices show the performance difference depending upon the spin-coating time, we monitored the change of film state with the spin-coating time. It should be mentioned here that the effect of substrate on the morphology of $CH_3NH_3PbI_3$ film is excluded because PEDOT:PSS layer is coated on the substrate before $CH_3NH_3PbI_3$ is deposited in device fabrication process. As shown in Fig. 2, the liquid film from DMF solution starts to solidify between 5–10 s after spin-coating. The color of liquid film before solidification is yellow (<5 s), which is the same color as the color of DMF bulk solution, and after solidification (≥ 10 s) the color changes from yellow to white and subsequently to brown. The color change by solidification is also observed in the film processed by DMSO solution. The color of film spin-coated from DMSO solution maintains yellow until 60 s of spin-coating time after which the color is changed to white due to solidification. It should be noted here that the liquid film from DMSO solution requires longer spin-coating time to solidify than DMF solution due to higher boiling temperature (189 ˚C) and lower vapor pressure (0.42 mmHg) than those of DMF (153 ˚C, 2.7 mmHg). Considering that the solidification during spin-coatng is closely

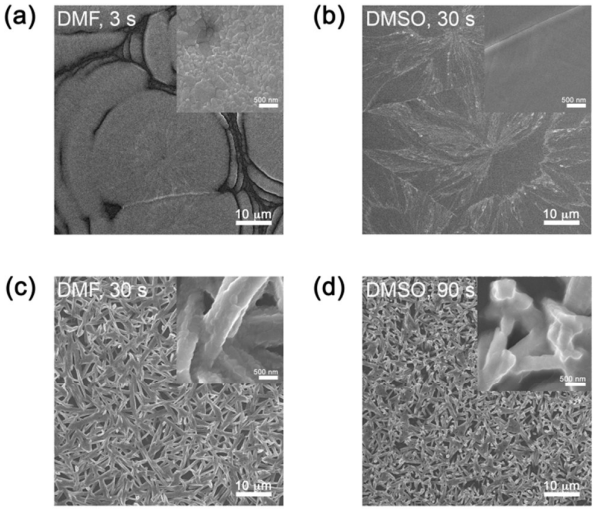

Fig. 4 SEM images of $CH_3NH_3PbI_3$ films with (a, b) flower-like and (c, d) tree-like morphology fabricated from (a, c) DMF and (b, d) DMSO solution. All films are thermally treated at 110 °C for 30 s immediately after spin-coating.

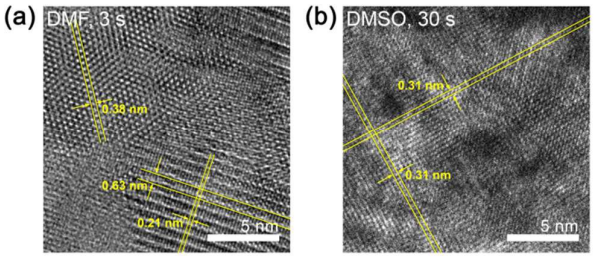

Fig. 5 HRTEM images of $CH_3NH_3PbI_3$ films with flower-like morphology. The films are spin-coated at 3000 rpm and are thermally treated at 110 °C for 30 s immediately after spin-coating.

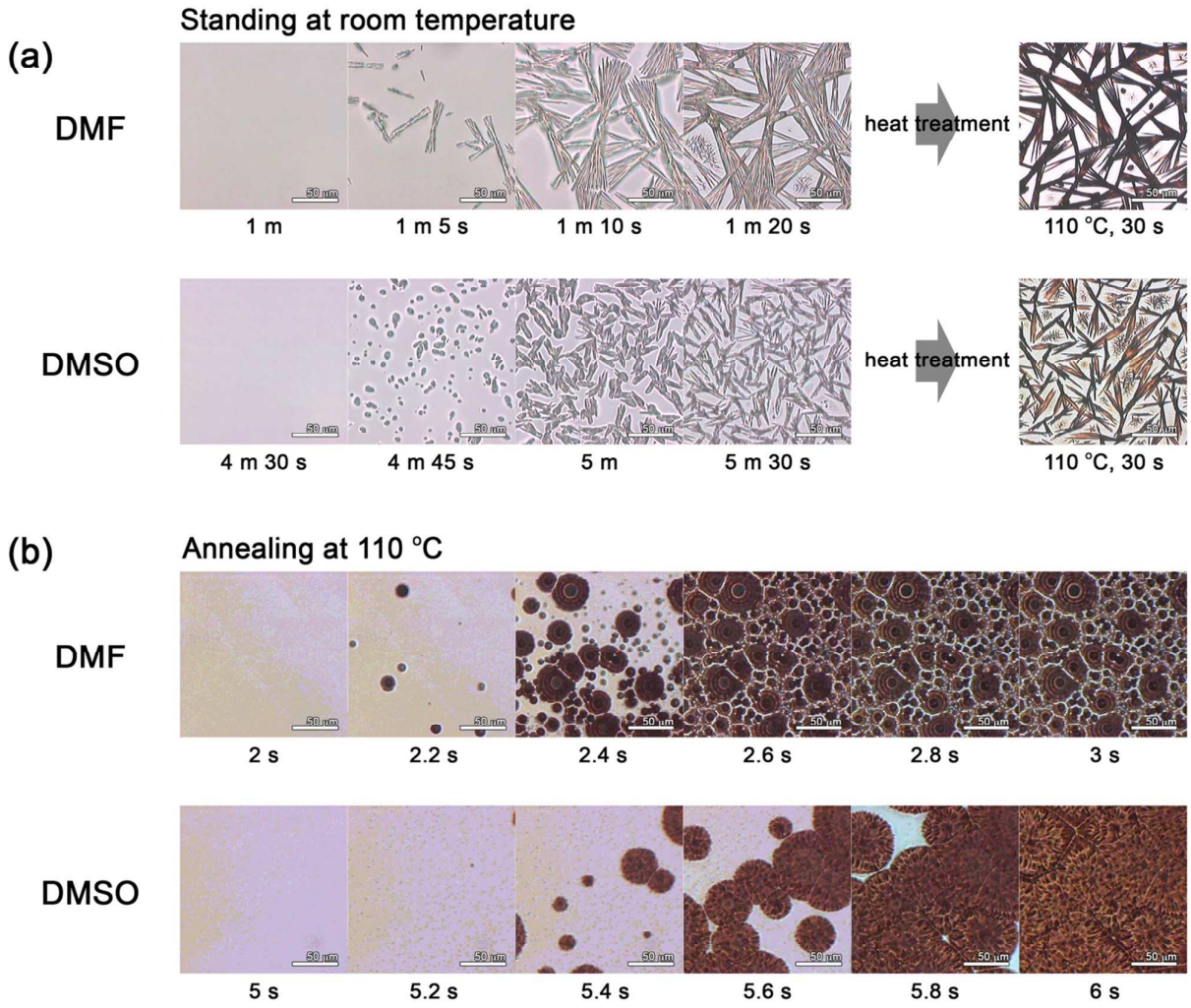

Fig. 6 In-situ OM images of crystal growth in liquid films (a) under room temperature and (b) at 110 ˚C. The liquid films prepared from DMF and DMSO solutions are spin-coated for 3 s and 30 s, respectively.

related to the device performance, it is concluded that the device performance becomes better when the spin-coating time is short so as to prevent solidification of liquid film during spin-coating.

When the films spin-coated for various spin-coating times are thermally treated at 110 ˚C for 30 s to complete the formation of $CH_3NH_3PbI_3$ solid film, the films show different morphologies depending upon the spin-coating time, as shown in optical microscopy (OM) images of Fig. 3. Independent of processing solvent, heat-treatment of liquid films develops the flower-like morphology with circular domain shape (Fig. 3a and 3e–3g), while the heat-treatment of films after solidification during spin-coating develops film morphology containing many pinholes (Fig. 3b–3d and 3h).

The microscopic morphologies of perovskite films as observed by scanning electron microscopy (SEM) also show that the films spin-coated for short time, which is not enough to solidify the liquid film, exhibit the flower-like morphology after heat-treatment (Fig. 4a and 4b) while the films spin-coated for longer times exhibit tree-like morphology containing many pinholes (Fig. 4c and 4d). Magnification of SEM images reveals that the crystal domains in all films are not composed of a single crystal but many micro-crystals (insets of Fig. 4). Another important feature is that the size of individual $CH_3NH_3PbI_3$ crystallites grown from DMSO solution is much larger than that grown from DMF solution. Especially, the film with flower-like morphology as developed from DMSO solution consists of large crystallites with the scale of tens of micrometers and good surface coverage. When the crystal morphologies of films are investigated by high-resolution transmission electron microscopy (HRTEM), as shown in Fig. 5, the HRTEM image of film with flower-like morphology, as developed from DMSO solution, reveals a large crystal plane with the lattice fringe indexed only as (004) plane, whereas the image of film with flower-like morphology fabricated from DMF solution shows multiple crystal planes such as (201) and (410). The multiple crystal planes indicate that the film fabricated from DMF solution is composed of smaller

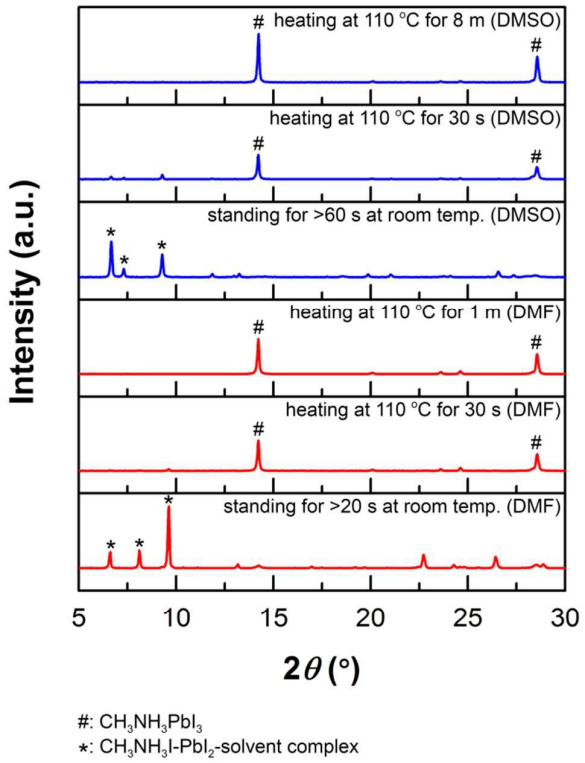

Fig. 7 XRD patterns of films fabricated from DMF and DMSO solution. Liquid films are solidified by standing the films at room temperature for >20 s (DMF) or >60 s (DMSO). The solidified films are thermally treated at 110 °C until the peaks of CH_3NH_3I–PbI_2–solvent complex disappear.

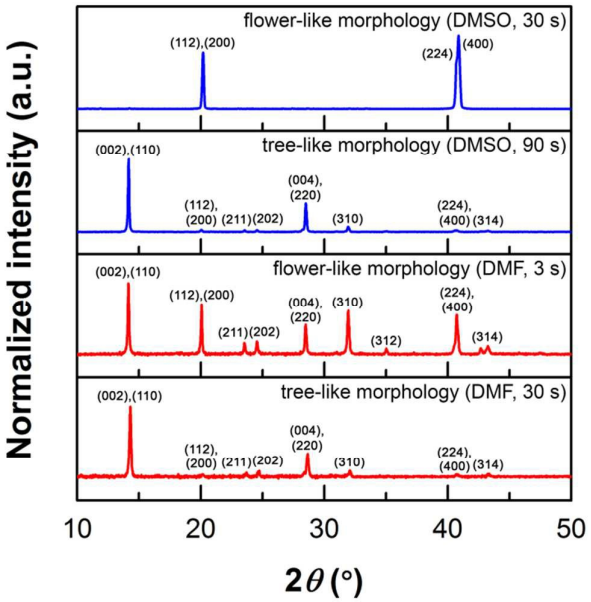

Fig. 8 XRD patterns of $CH_3NH_3PbI_3$ films with flower-like and tree-like morphology as prepared from DMF and DMSO solution. All films are thermally treated at 110 °C for 30 s immediately after spin-coating.

$CH_3NH_3PbI_3$ crystallites with different crystal orientation (Fig. 5a), while the HRTEM image of film from DMSO solution exhibits only one crystal plane (Fig. 5b). This is a direct evidence that the crystallites in the film fabricated from DMSO solution are much larger in crystal size than the crystallites in the film fabricated from DMF solution, although the two films show flower-like morphology.

The above observation leads us to conclude that long spin-coating time enough to solidify the liquid film develops tree-like morphology with many pinholes which may provide shunting pathway and thus reduce the solar cell efficiency, while short spin-coating time not enough to solidify during spin-coating develops flower-like morphology with good film coverage which affords high photovoltaic performance. Specifically, when the film with flower-like morphology, as spin-coated for short time (15 s) from DMSO solution, is used as active layer, the device exhibits much higher PCE (13.85%) than the device (PCE=0.22%) fabricated by spin-coating of DMSO solution for long time (90 s). The higher efficiency of the device fabricated from short-time spin-coating of DMSO solution may arise from larger crystal size and preferred crystal orientation in the film (which will be discussed in the next section), which facilitates the charge transport and reduces defect density. To reveal the reason for high efficiency of the device with flower-like morphology, we measured bulk recombination times of devices using an impedance analyzer.[18]

Devices with flower-like morphology show longer bulk recombination time (which may afford higher efficiency) than devices with tree-like morphology (Figure S8) probably due to larger crystal size of flower-like morphology, indicating that the charge recombination in the bulk film is closely related to the film morphology.

To reveal the origin for the difference between tree-like and flower-like morphologies, the development of morphology in liquid films, prepared by controlling the spin-coating time (3 s for DMF solution and 30 s for DMSO solution) to prevent solidification, is monitored by in-situ OM, as shown in Fig. 6 (see also video files in electronic supplementary information). When the liquid film from DMF solution is dried at room temperature, the colorless crystals start to grow at 60 s of standing and grow slowly for the next 20 s. When the dried film was heat-treated at 110 ˚C, the color of crystals is changed from colorless to dark brown, retaining the tree-like morphology. The same phenomenon is also observed in the film spin-coated from DMSO solution at room temperature, indicating that the tree-like morphology is developed by growth of colorless crystals (Fig. 6a). However, when liquid films spin-coated from both DMF and DMSO solutions are heat-treated at 110 ˚C immediately after short spin-coating times, the color of nuclei is dark brown and the crystals rapidly grow in circular shape (Fig. 6b).

When the crystal structure of colorless crystals in the film dried at room temperature was identified by X-ray diffraction (XRD), as shown in Fig. 7, the XRD pattern of dried film from DMSO solution exhibits several primary peaks between 5–10˚, which are the same as the diffraction peaks of CH_3NH_3I–PbI_2–DMSO complex,[29] indicating that the colorless crystals are

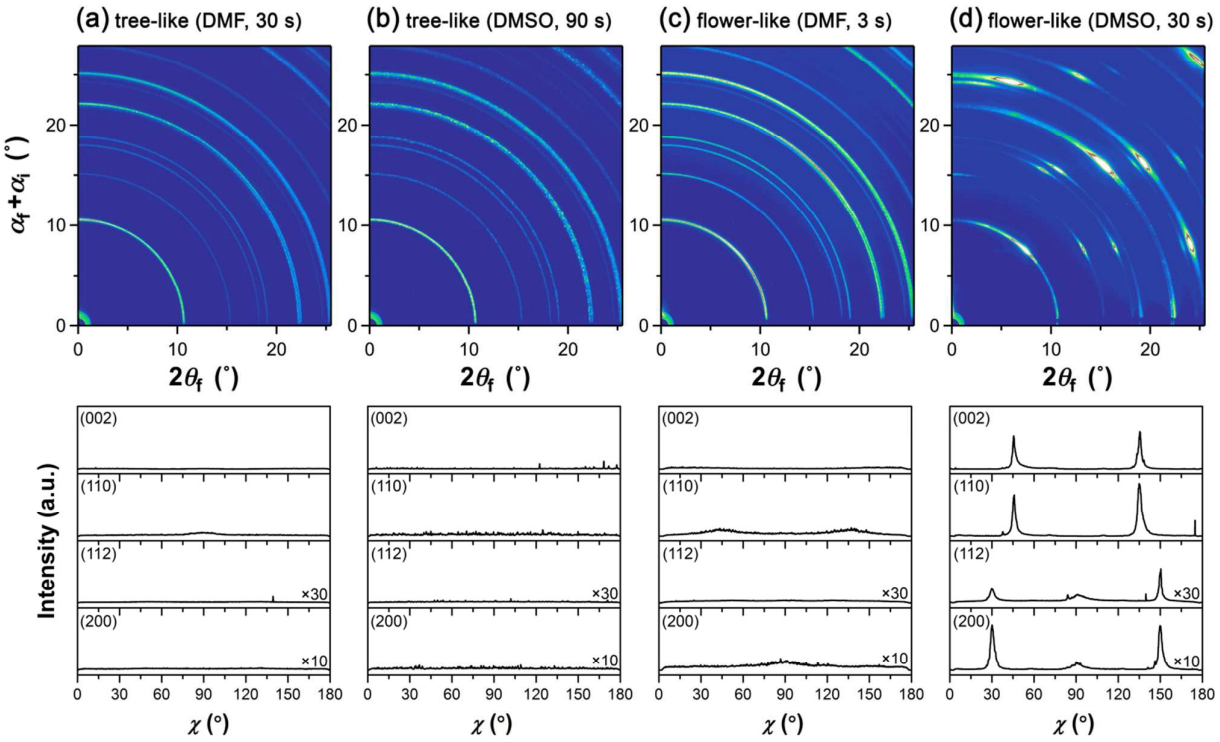

Fig. 9 2D GIXD patterns of $CH_3NH_3PbI_3$ films with (a, b) tree-like and (c, d) flower-like morphologies fabricated from (a, c) DMF and (b, d) DMSO solution. All films are thermally treated at 110 °C for 30 s after spin-coating.

formed from CH_3NH_3I–PbI_2–DMSO complex. However, the crystal structure of CH_3NH_3I–PbI_2–DMF complex has not been reported, although it was reported that DMF molecule coordinates to Pb in PbI_2 to form PbI_2–DMF complex[31] and the XRD pattern of PbI_2–DMF complex crystal was also reported.[32] Since the XRD pattern of film dried from DMF is different from the reported XRD pattern of PbI_2–DMF complex crystal, the colorless crystals formed from DMF solution should not be the crystals of PbI_2–DMF complex. Fourier transform infrared spectra (Fig. S9) provide another evidence of complex formation of CH_3NH_3I–PbI_2–solvent: Vibration peaks of C=O of DMF and S=O of DMSO in spectra of PbI_2–solvent complexes are shifted to shorter wavenumber as compared with the corresponding peaks of pure DMF and DMSO due to interaction between PbI_2 and solvent molecule, and the vibration peaks in spectra of CH_3NH_3I–PbI_2–solvent complexes are further shifted because both CH_3NH_3I and PbI_2 interact with solvent molecule.[33] Hence it is reasonable to assume that the colorless crystals are the crystals of CH_3NH_3I–PbI_2–DMF complex. When the crystals of CH_3NH_3I–PbI_2–solvent complexes are heated at 110 ˚C, the (110) peak of $CH_3NH_3PbI_3$ at 14.2˚ grows while the diffraction peaks of complex crystals between 5–10˚ disappear accompanying by the color change from colorless to dark brown in in-situ OM images (Fig. 6a). Furthermore, formation of the complex crystals can also be identified in XRD patterns of the films as solidified during spin-coating (compare Fig. 7 with Fig. S3), indicating that the crystals of CH_3NH_3I–PbI_2–solvent complexes are formed by solidification during spin-coating. Therefore, it can be concluded that the crystals of CH_3NH_3I–PbI_2–solvent complexes are formed when the solidification occurs during spin-coating or when the liquid films after short spin-coating time are placed at room temperature for long time and that the crystals of the complexes grow in one-dimensional direction, leading to tree-like morphology of $CH_3NH_3PbI_3$ crystals.

The color change of CH_3NH_3I–PbI_2–solvent complex crystal during heat treatment at 110 °C is due to evaporation of solvent molecules which participated in the complex formation. However, when the liquid films after short spin-coating time are heat-treated at 110 °C, $CH_3NH_3PbI_3$ crystals (flower-like morphology) are directly formed without formation of complex crystals, because solvent molecules are evaporated before the complex crystals are formed. When the liquid film is annealed at different temperatures, tree-like morphology is developed at 60 °C annealing, and flower-like morphology is developed at 100 °C. Mixed morphology of tree-like and flower-like morphologies is developed at 80 °C probably due to the competition between formation of CH_3NH_3I–PbI_2–solvent complex crystal and solvent evaporation without formation of complex crystal (Fig. S4).

$CH_3NH_3PbI_3$ crystal orientation

The above observation tells us that the crystal formation of CH_3NH_3I–PbI_2–solvent complex is closely related to the film

morphology and the orientation of $CH_3NH_3PbI_3$ crystallites.

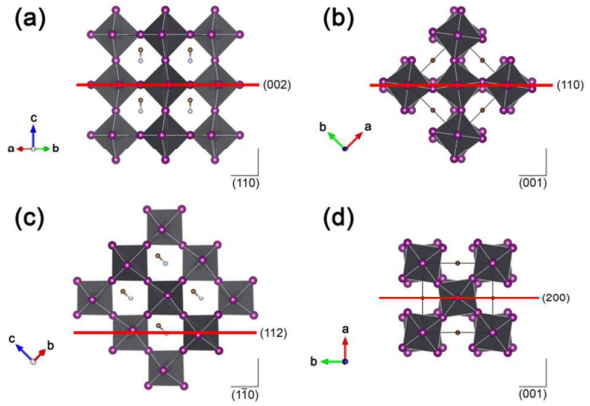

Fig. 10 Unit cell of tetragonal $CH_3NH_3PbI_3$ crystal. The C, N, I and Pb atoms are represented as brown, light blue, purple and black spheres, respectively, and black octahedrons represent PbI_6 units. Solid lines indicate (a) (002), (b) (110), (c) (112) and (d) (200) planes.

Considering the fact that the same crystal structure, corresponding to the tetragonal structure of $CH_3NH_3PbI_3$ perovskite, is observed in the powder XRD patterns of all films (Fig. S5), the difference between thin-film XRD patterns (Fig. 8) indicates that $CH_3NH_3PbI_3$ crystallites have different orientation depending on the film morphology. The XRD patterns of films with tree-like morphology show strong (002) and (110) peaks dominantly while the patterns of films with flower-like morphology exhibit strong (112) and (200) peaks.

The crystal orientation in $CH_3NH_3PbI_3$ films can clearly be identified by 2D grazing incidence X-ray diffraction (GIXD) and its azimuthal angle (χ) scans (Fig. 9). The $CH_3NH_3PbI_3$ crystallites in the films with tree-like morphologies, as prepared from DMF and DMSO solutions, do not show preferential orientation (Fig. 9a and 9b) while the crystallites in the films with flower-like morphology are preferentially oriented along (112) or (200) directions to the substrate (Fig. 9c and 9d). Especially, the film from DMSO solution exhibits spot-like reflections with strong intensity, indicating that the $CH_3NH_3PbI_3$ crystallites are highly oriented. Since the edges of PbI_6 octahedron in $CH_3NH_3PbI_3$ crystal contact with the substrate (see Fig. 10), indicating that $CH_3NH_3PbI_3$ crystallites are oriented along (112) or (200) directions, the crystals with flower-like morphology are oriented in such a way that edges of PbI_6 octahedron contact with the substrate. This result leads us to conclude that the orientation of $CH_3NH_3PbI_3$ crystals is strongly dependent on the film morphology, which can be easily controlled by varying the spin-coating condition. Considering that preferential orientation of perovskite crystals affords high PCEs, the crystal orientation must be one of important factors determining the solar cell performance, although the effect of crystal orientation on photovoltaic properties of $CH_3NH_3PbI_3$ perovskite has not been fully understood and therefore further studies should be needed to reveal the orientation effect.

Conclusions

We have investigated the effect of solidification during spin-coating in one-step deposition on the morphology of $CH_3NH_3PbI_3$ film and its photovoltaic performance. In-situ OM and XRD studies reveal that the solidification during spin-coating is accompanied by formation of CH_3NH_3I–PbI_2–solvent complex crystals, which induces the crystal growth in one-dimensional direction. The crystal growth in one-dimensional direction yields tree-like morphology with many pinholes in $CH_3NH_3PbI_3$ perovskite film, resulting in very low PCEs of solar cell devices. However, when the solidification during spin-coating is suppressed by shortening the spin-coating time and thereafter $CH_3NH_3PbI_3$ is crystallized directly from the liquid film after spin-coating by post heat-treatment, flower-like morphology is developed in the film with high surface coverage and large crystal size. Specifically, the film from DMSO solution showing flower-like morphology has large-sized crystallites on the length scale of tens of micrometers and the crystallites in the film are highly orientated along (112) and (200) directions, resulting in a high PCE of 13.85%. This observation demonstrates that the solidification accompanied by complex formation during spin-coating should be avoided for high performance perovskite solar cells. Hence, the direct crystallization from liquid film without formation of the complex crystal is a promising method for achieving high performance perovskite solar cells.

Experimental

Substrate preparation

ITO (10 Ω sq^{-1}, KETI) coated glass was cleaned by stepwise sonication in acetone and IPA for 30 min each. After complete drying, the ITO coated glass was treated with UV–ozone for 15 min. PEDOT:PSS (Heraeus Clevios P VP AI 4083) was spin-coated on the ITO with 40 nm in thickness and the substrate was annealed at 150 °C for 20 min in ambient condition.

Fabrication of perovskite solar cells

$CH_3NH_3PbI_3$ and $PC_{61}BM$ layers were deposited in a N_2-filled glove box. DMF and DMSO precursor solutions was spin-coated on the PEDOT:PSS at 3000 rpm. The substrate spin-coated with precursor solution was immediately transferred on a hot plate and heated at 110 °C for 30 s. $PC_{61}BM$ was then spin-coated on the $CH_3NH_3PbI_3$ layer at 3000 rpm. Finally, calcium (25 nm) and aluminum cathode (100 nm) was thermally evaporated under vacuum ($<10^{-6}$ Torr) on the $PC_{61}BM$ layer through a shadow mask to give a device area of 0.1 cm^2.

Characterization

In-situ OM images were obtained by Leica MPS 30 microscope and SEM images were obtained by JSM-6700F (JEOL). XRD patterns of powder and films were obtained by X-ray diffractometer (D8 Advance, Bruker) using Cu-K$\alpha_{1,2}$ radiation (λ= 1.5418 Å) at a scan rate of 2° min^{-1}. GIXD measurements

were performed at 6D C&S UNIST-PAL beam-line of Pohang Accelerator Laboratory in Korea. The X-rays coming from the in-vacuum undulator are monochromated (wavelength, λ =1.2398 Å) using a Si(111) double-crystal monochromator and focused horizontally and vertically (300 (H)×30 (V) μm^2 in FWHM @sample position) using K-B type mirror system. GIXD sample stage is equipped with a 7-axis motorized stage for the fine alignment of sample and the incidence angle of X-ray beam was set to 0.2°. GIXD patterns were recorded with a 2D CCD detector and X-ray irradiation time was 120 second. Diffraction angles were calibrated by a pre-calibrated sucrose (Monoclinic, *P*21, a = 10.8631 Å, b = 8.7044 Å, c = 7.7624 Å, b = 102.938°) and the sample-to-detector distance was about 235.5 mm. *J–V* curves of photovoltaic cells were obtained using a computer-controlled Keithley 4200 source measurement unit under AM 1.5G (100 mW cm^{-2}) simulated by an Oriel solar simulator (Oriel 91160A). The light intensity was calibrated using a NREL-certified photodiode prior to each measurement. The EQE was measured using Polaronix K3100 IPCE measurement system (McScience). The light intensity at each wavelength was calibrated with a standard single-crystal Si cell. JASCO FT-IR-660 plus was used to collect FT-IR spectra. The spectra of DMF and DMSO were measured in liquid phase and the specra of PbI_2–DMF, CH_3NH_3I–PbI_2–DMF, PbI_2–DMSO and CH_3NH_3I–PbI_2–DMSO were measured in powder samples using KBr pellet. Impedance spectroscopic measurements were carried out using an impedance analyzer (Bio-Logic VMP3) with various potential from 0 to 0.8 V in dark. AC 10 mV perturbation was applied with a frequency from 1 MHz to 100 Hz. The obtained spectra were fitted with EC-Lab software.

Acknowledgements

The authors thank the Ministry of Education, Korea for financial support through Global Research Laboratory (GRL). Experiment at the PLS-II 6D` C&S UNIST-PAL beamline was supported in part by MIST and POSTECH. The authors also thank Dr. Hyungju Ahn for GIXD measurement.

Notes and references

1 N. K. Noel, S. D. Stranks, A. Abate, C. Wehrenfennig, S. Guarnera, A.-A. Haghighirad, A. Sadhanala, G. E. Eperon, S. K. Pathak, M. B. Johnston, A. Petrozza, L. M. Herz and H. J. Snaith, *Energy Environ. Sci*., 2014, **7**, 3061.
2 F. Hao, C. C. Stoumpos, D. H. Cao, R. P. H. Chang and M. G. Kanatzidis, *Nat. Photonics*, 2014, **8**, 489.
3 G. Xing, N. Mathews, S. Sun, S. S. Lim, Y. M. Lam, M. Grätzel, S. Mhaisalkar and T. C. Sum, *Science*, 2013, **342**, 344.
4 J.-W. Lee, D.-J. Seol, A.-N. Cho and N.-G. Park, *Adv. Mater*., 2014, **26**, 4991.
5 S. D. Stranks, G. E. Eperon, G. Grancini, C. Menelaou, M. J. P. Alcocer, T. Leijtens, L. M. Herz, A. Petrozza and H. J. Snaith, *Science*, 2013, **342**, 341.
6 E. Edri, S. Kirmayer, A. Henning, S. Mukhopadhyay, K. Gartsman, Y. Rosenwaks, G. Hodes and D. Cahen, *Nano Lett*., 2014, **14**, 1000.
7 V. D'Innocenzo, G. Grancini, M. J. P. Alcocer, A. R. S. Kandada, S. D. Stranks, M. M. Lee, G. Lanzani, H. J. Snaith and A. Petrozza, *Nat. Commun*., 2014, **5**, 3586.
8 M. Hirasawa, T. Ishihara, T. Goto, K. Uchida and N. Miura, *Physica B*, 1994, **201**, 427.
9 K. Tanaka, T. Takahashi, T. Ban, T. Kondo, K. Uchida and N. Miura, *Solid State Commun*., 2003, **127**, 619.
10 T. Leijtens, S. D. Stranks, G. E. Eperon, R. Lindblad, E. M. J. Johansson, I. J. McPherson, H. Rensmo, J. M. Ball, M. M. Lee and H. J. Snaith, *ACS Nano*, 2014, **8**, 7147.
11 C. Wehrenfennig, G. E. Eperon, M. B. Johnston, H. J. Snaith and L. M. Herz, *Adv. Mater*., 2014, **26**, 1584.
12 A. Kojima, K. Teshima, Y. Shirai and T. Miyasaka, *J. Am. Chem. Soc*., 2009, **131**, 6050.
13 H. Zhou, Q. Chen, G. Li, S. Luo, T.-b. Song, H.-S. Duan, Z. Hong, J. You, Y. Liu and Y. Yang, *Science*, 2014, **345**, 542.
14 G. E. Eperon, V. M. Burlakov, P. Docampo, A. Goriely and H. J. Snaith, *Adv. Funct. Mater*., 2014, **24**, 151.
15 M. Xiao, F. Huang, W. Huang, Y. Dkhissi, Y. Zhu, J. Etheridge, A. Gray-Weale, U. Bach, Y.-B. Cheng and L. Spiccia, *Angew. Chem. Int. Ed*., 2014, **53**, 9898.
16 H. J. Snaith, A. Abate, J. M. Ball, G. E. Eperon, T. Leijtens, N. K. Noel, S. D. Stranks, J. T.-W. Wang, K. Wojciechowski and W. Zhang, *J. Phys. Chem. Lett*., 2014, **5**, 1511.
17 H.-S. Kim and N.-G. Park, *J. Phys. Chem. Lett*., 2014, **5**, 2927.
18 Y. Shao, Z. Xiao, C. Bi, Y. Yuan and J. Huang, *Nat. Commun*., 2014, **5**, 5784.
19 J. Burschka, N. Pellet, S.-J. Moon, R. Humphry-Baker, P. Gao, M. K. Nazeeruddin and M. Grätzel, *Nature*, 2013, **499**, 316.
20 M. Liu, M. B. Johnston and H. J. Snaith, *Nature*, 2013, **501**, 395.
21 H.-B. Kim, H. Choi, J. Jeong, S. Kim, B. Walker, S. Song and J. Y. Kim, *Nanoscale*, 2014, **6**, 6679.
22 J.-Y. Jeng, Y.-F. Chiang, M.-H. Lee, S.-R. Peng, T.-F. Guo, P. Chen and T.-C. Wen, *Adv. Mater*., 2013, **25**, 3727.
23 J. H. Heo, D. H. Song and S. H. Im, *Adv. Mater*., 2014, **26**, 8179.
24 C.-C. Chueh, C.-Y. Liao, F. Zuo, S. T. Williams, P.-W. Liang and A. K.-Y. Jen, *J. Mater. Chem. A*, 2015, **3**, 9058.
25 P.-W. Liang, C.-Y. Liao, C.-C. Chueh, F. Zuo, S. T. Williams, X.-K. Xin, J. Lin and A. K.-Y. Jen, *Adv. Mater*., 2014, **26**, 3748.
26 C.-C. Chen, Z. Hong, G. Li, Q. Chen, H. Zhou and Y. Yang, *J. Photon. Energy*, 2015, **5**, 057405.
27 C. Zuo and L. Ding, *Nanoscale*, 2014, **6**, 9935.
28 X. Song, W. Wang, P. Sun, W. Ma and Z.-K. Chen, *Appl. Phys. Lett*., 2015, **106**, 033901.
29 N. J. Jeon, J. H. Noh, Y. C. Kim, W. S. Yang, S. Ryu and S. I. Seok, *Nat. Mater*., 2014, **13**, 897.
30 J. Seo, S. Park, Y. C. Kim, N. J. Jeon, J. H. Noh, S. C. Yoon and S. I. Seok, *Energy Environ. Sci*., 2014, **7**, 2642.
31 A. Wakamiya, M. Endo, T. Sasamori, N. Tokitoh, Y. Ogomi, S. Hayase and Y. Murata, *Chem. Lett*., 2014, **43**, 711.
32 D. Shen, X. Yu, X. Cai, M. Peng, Y. Ma, X. Su, L. Xiao and D. Zou, *J. Mater. Chem. A*, 2014, **2**, 20454.
33 N. Ahn, D.-Y. Son, I.-H. Jang, S. M. Kang, M. Choi and N.-G. Park, *J. Am. Chem. Soc*., 2015, **137**, 8696.

Table of contents

Two different mechanisms of $CH_3NH_3PbI_3$ film formation in one-step deposition and its effect on photovoltaic properties of OPV-type perovskite solar cells

Seunghwan Bae,[a] Seung Jin Han,[a] Tae Joo Shin,[b] and Won Ho Jo*[a]

[a]*Department of Materials Science and Engineering, Seoul National University, 1 Gwanak-ro, Gwanak-gu, Seoul 151-744, Korea*

[b]*Pohang Accelerator Laboratory, Pohang, Kyungbuk 790-784, Korea*

Two different morphologies of perovskite, tree-like and flower-like morphologies, are developed depending upon the spin-coating time and post-heat treatment temperature.